Evaluation of Current Ripple Amplitude in Three-Phase PWM Voltage Source Inverters

G. Grandi, J. Loncarski
Department of Electrical, Electronic and Information Engineering
Alma Mater Studiorum - University of Bologna, Italy
gabriele.grandi@unibo.it, jelena.loncarski2@unibo.it

Abstract — **Determination of current ripple in three-phase PWM voltage source inverters (VSI) is important for both design and control purposes, since this is the most popular conversion topology for energy conversion systems. In this paper the complete analysis of the peak-to-peak current ripple distribution over a fundamental period is given for three-phase VSIs. In particular, peak-to-peak current ripple amplitude is analytically determined as a function of the modulation index. Minimum, maximum, and average values are also emphasized. Although the reference is made to continuous symmetric PWM, being the most simple and effective solution to minimize the current ripple, the analysis could be easily extended to either discontinuous or unsymmetrical modulation, both carrier-based and space vector PWM. The analytical developments for all the different subcases are verified by numerical simulations.**

I. INTRODUCTION

Three-phase voltage source inverters (VSIs) are widely utilized in ac motor drives, controlled rectifiers, and in general grid-connected applications as a means of dc-ac power conversion devices. Most of VSI applications employ carrier-based PWM (CB-PWM) control schemes due to their simplicity of implementation, both in analog and digital ways, fixed switching frequency and well defined harmonic spectrum characteristics [1]. Furthermore, switching losses are easier to control with constant switching frequency, and the inverter design can take advantage of an accurate losses calculation. Different types of CB-PWM and space vector PWM (SV-PWM) are investigated and optimal solutions are proposed with reference to reducing the current ripple and switching losses [2]-[4]. It should be underlined here that CB-PWM leads to equivalent switching patterns as SV-PWM by proper zero-sequence modulating signal injection [5].

A complete analysis of three-phase PWM converter system addressed switching losses, dc link harmonics, and inverter input/output harmonics is given by [6]. It has been shown that reduction of the output current harmonics in case of continuous PWM can be achieved by proper zero-sequence signal injection. A further reduction of the rms value of the current ripple is possible in some cases by development of discontinuous PWM schemes, which allow increasing the carrier frequency while maintaining the switching losses as same as continuous PWM. In the case of a loss minimization, two cases are observed in [7], which correspond to the continuous and to the discontinuous modulation as can be seen by comparing the dependencies of the normalized harmonic power losses on the converters modulation index.

An analytical approach for the analysis of current ripple in SV-PWM controlled induction motor drives has been presented in [8], where is proposed optimal SVM technique with calculation of the duty-cycles of the two zero voltage vectors, and then the switching pattern of the optimal SVM technique.

Newer studies on output current ripple rms in multiphase drives are presented in [9], [10], where a five-phase system is considered. Due to existence of more planes (two 2-D planes for five-phase systems), the concept of harmonic flux is used to mitigate initially the dependencies on the equivalent inductances in each plane, where current ripple occurs. In [11] an attempt to evaluate the output current ripple of a five-phase inverter has been reported, but only a single adjacent polygon connection has been encompassed by the analysis. As a consequence, flux harmonic distortion factor (HDF) values and squared rms current ripple values are only part of the complete solution rather than the total HDF and total squared rms current ripple.

Analysis of current ripple in a sub-period is given in [12], [13], as the error volt-second quantities which are the errors between instantaneous applied and reference voltage vectors. Of interest was to study the current ripple rms over a sub-period and to utilize this knowledge to design hybrid PWM techniques, which reduces the line current distortion. Current ripple rms is also analyzed in [14], for three-phase inverted feeding passive load. The analysis are conducted on one switching period and of interest was to derive rms value of output current ripple as function of modulation index.

The importance of current ripple amplitude (peak-to-peak) is recognized in [15], where ripple is analyzed by introducing Thévenin equivalent circuit of the 8 different voltage vectors. In general, the evaluation of current ripple allows adjusting the switching frequency for certain ripple requirements. As an example, the knowledge of current ripple distribution over a fundamental period can be useful to determine multiple zero-crossing intervals of output current, in order to evaluate the modified output voltage distortion introduced by dead-times for high ripple currents [16]. Furthermore, on the basis of both current ripple and fundamental current component amplitudes, maximum instantaneous peak current can be determined, allowing a proper setup of thresholds and protection circuitries, with the possibility of a more detailed design of current-limited power components.

In this paper the complete analysis of peak-to-peak output current ripple is further developed for three-phase PWM inverters, with reference to continuous symmetric PWM, either carrier-based or space vector PWM. Detailed analytical expressions of peak-to-peak current ripple distribution over a fundamental period are given as function of the modulation index. In addition, maximum and minimum of the peak-to-

978-1-4673-4913-0/13/$31.00 ©2013 IEEE

peak current ripple are evaluated by introducing simplified and effective expressions. Although the instantaneous current ripple is defined for both grid connected applications and ac motor drives, the analysis can be applied to passive loads as well. All the analytical developments are verified by numerical simulations on a realistic circuit model, implemented by the Simulink tool of Matlab.

II. Evaluation of Peak-to-Peak Current Ripple Amplitude

A. Load model and current ripple definitions

Basic voltage equation for inverter supplying a motor or connected to grid, as summarized in Fig. 1, can be written for each phase as

$$v(t) = R\,i(t) + L\frac{di}{dt} + v_g(t)\,. \tag{1}$$

Eq. (1) can be averaged over the switching period T_s leading to

$$\bar{v}(T_s) = R\,\bar{i}(T_s) + \frac{L\,\Delta i}{T_s} + \bar{v}_g(T_s)\,, \tag{2}$$

being $\Delta i = i(T_s) - i(0)$. (3)

The alternating component of inverter voltage can be written by introducing the average over the switching period as

$$\tilde{v}(t) = v(t) - \bar{v}(T_s)\,. \tag{4}$$

By introducing (1) and (2) in (4) leads to

$$\tilde{v}(t) = R\left[i(t) - \bar{i}(T_s)\right] + L\left[\frac{di}{dt} - \frac{\Delta i}{T_s}\right] + \left[v_g(t) - \bar{v}_g(T_s)\right]. \tag{5}$$

The first and the third (last) term in (5) can be usually neglected leading to

$$\tilde{v}(t) = L\left[\frac{di}{dt} - \frac{\Delta i}{T_s}\right]. \tag{6}$$

The current variation in the sub-period $[0 - t]$, also depicted in Fig. 2, can be calculated from (6) as

$$\Delta i(t) = \frac{1}{L}\int_0^t \tilde{v}(t)dt + \frac{t}{T_s}\Delta i\,. \tag{7}$$

Eq. (7) allows to define the instantaneous current ripple as

$$\tilde{i}\,(t) = \Delta i(t) - \frac{t}{T_s}\Delta i = \frac{1}{L}\int_0^t \tilde{v}(t)dt\,. \tag{8}$$

Finally, the peak-to-peak current ripple can be defined as

$$\tilde{i}_{pp} = max\left\{\tilde{i}\,(T_s)\right\} - min\left\{\tilde{i}\,(T_s)\right\}. \tag{9}$$

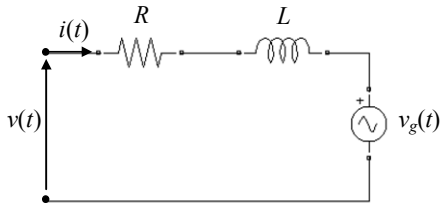

Fig. 1. Basic circuit model for one phase.

B. Space vector PWM equations

The SV-PWM of three-phase inverters is based on the determination of application times of active and null inverter voltage vectors $\boldsymbol{v}$ in every switching period T_s. In case of symmetric SV-PWM, the sequence is determined in $T_s/2$ and symmetrically repeated in the next half switching period. By equally sharing the application time of the null voltage vector between the switch configurations 000 and 111, the so called "centered" switching pattern is realized and nearly-optimal modulation able to minimize the RMS of current ripple is obtained [8]. As result of the SV-PWM, for each phase, the average of the inverter output voltage $\bar{v}(T_s)$ corresponds to the reference voltage v^*.

In the case of sinusoidal balanced output voltages supplying a balanced load, the reference output voltage vector is $\boldsymbol{v}^* = m\,V_{dc}\,exp(j\vartheta)$, being m the modulation index and V_{dc} the dc bus voltage, $m = V^*/V_{dc}$. Reference is made to Fig. 3. In this case, SV modulation is quarter-wave symmetric, so it can be analyzed in the range [0, 90°] of the phase angle $\vartheta = \omega t$. In particular, the two ranges $0 \le \vartheta \le 60°$, and $60° \le \vartheta \le 90°$can be considered.

In the range $0 \le \vartheta \le 60°$, the application times are

$$t_1 = m\sqrt{3}\,\frac{T_s}{2}\,sin(60° - \vartheta)\,, \tag{10}$$

$$t_2 = m\sqrt{3}\,\frac{T_s}{2}\,sin\,\vartheta\,, \tag{11}$$

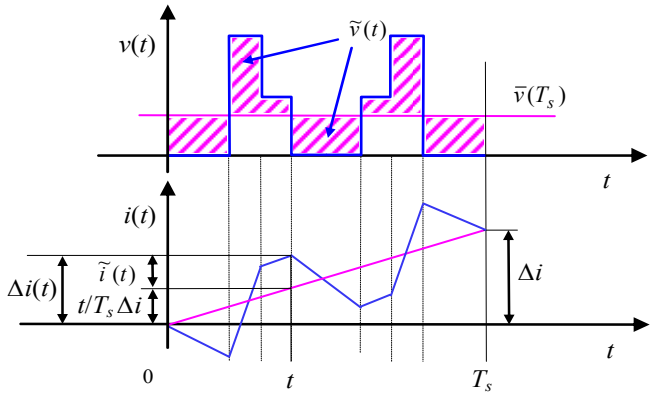

Fig. 2. Details of generic output voltage and current in the switching period.

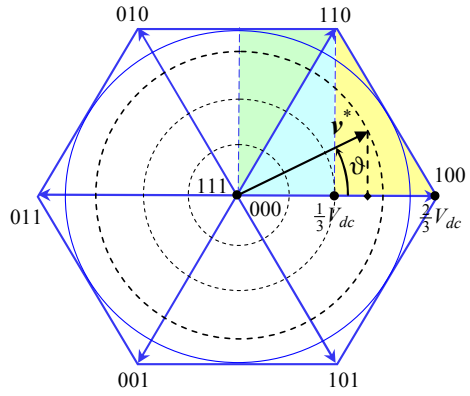

Fig. 3. Space vector diagram of inverter output voltage with six sectors and the three identified triangles. Dashed circles represent m = 1/6, 1/3, 1/2.

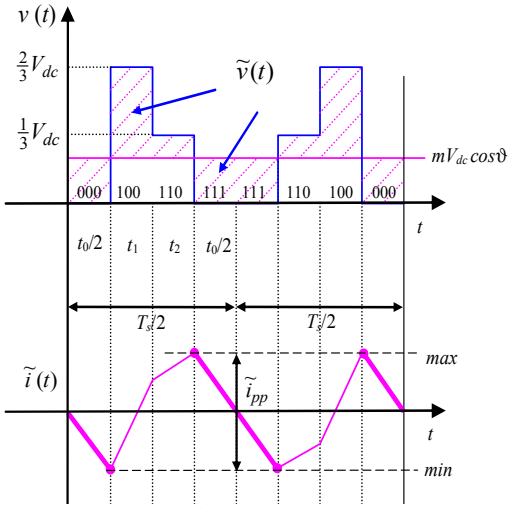

Fig. 4. Output voltage and current ripple in one switching period ($0 \le \vartheta \le 60°$, $0 \le m\cos\vartheta \le 1/3$).

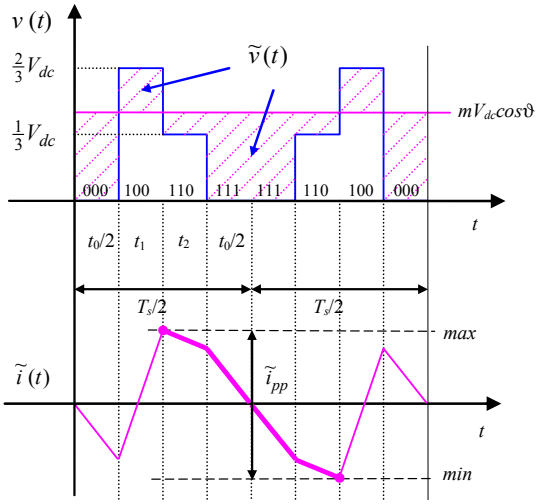

Fig. 5. Output voltage and current ripple in one switching period ($0 \le \vartheta \le 60°$, $m\cos\vartheta > 1/3$).

$$t_0 = \frac{T_s}{2} - (t_1 + t_2) = \frac{T_s}{2}\left[1 - \sqrt{3} m \sin(60^\circ + \vartheta)\right] \quad (12)$$

In the range $60° \le \vartheta \le 90°$, the application times are

$$t_1 = m\sqrt{3}\frac{T_s}{2}\sin(120^\circ - \vartheta)\,, \quad (13)$$

$$t_2 = m\sqrt{3}\frac{T_s}{2}\sin(\vartheta - 60^\circ)\,, \quad (14)$$

$$t_0 = \frac{T_s}{2} - (t_1 + t_2) = \frac{T_s}{2}\left[1 - \sqrt{3} m \sin\vartheta\right], \quad (15)$$

Note that the modulation limit is $m \le m_{max} = 1/\sqrt{3}$, according to the generalized expression given in [17] for n phases, $m_{max} = [2\cos(\pi/2n)]^{-1}$.

C. Ripple evaluation

Due to the symmetry among the three phases in the considered case of sinusoidal balanced currents, only the first phase is examined in the following analysis. In terms of space vectors, the variables of the first phase are given by the projection of the corresponding space vectors on the real axes. In particular, the average output voltage is given by

$$\bar{v}(T_s) = v^* = Re\{\mathbf{v}^*\} = V^*\cos\vartheta = V_{dc} m \cos\vartheta\,. \quad (16)$$

By introducing (16) in (4), the alternative component of inverter output voltage of the first phase can be written as

$$\tilde{v}(t) = \left[S_1 - \frac{1}{3}(S_1 + S_2 + S_3)\right] V_{dc} - m V_{dc}\cos\vartheta\,, \quad (17)$$

being $S_k = [0, 1]$ the switch state of the k-th inverter leg. In order to evaluate the current ripple in the whole phase angle range $0 < \vartheta < 90°$, the three different triangles depicted in Fig. 3 must be separately considered.

1) Evaluation in the range $0 \le \vartheta \le 60°$

Considering the first sector of the hexagon, $0 \le \vartheta \le 60°$, we can distinguish two different cases, when $0 \le m\cos\vartheta \le 1/3$ and $m\cos\vartheta \ge 1/3$, corresponding to the two colored triangular regions in Fig. 3.

For modulation index $0 \le m\cos\vartheta \le 1/3$, the current ripple $\tilde{i}$ and its peak-to-peak value $\tilde{i}_{pp}$ are depicted in Fig. 4, together with the instantaneous output voltage $v(t)$. According to Fig. 4, $\tilde{i}_{pp}$ can be evaluated by (8), (9), and (17), considering application interval t_0 (light blue area in Fig. 3), leading to

$$\tilde{i}_{pp} = \frac{1}{L}\{V_{dc} m \cos\vartheta\ t_0\}. \quad (18)$$

The case of $1/3 \le m\cos\vartheta \le 1/\sqrt{3}$ is depicted in Fig. 5. In this case $\tilde{i}_{pp}$ can be evaluated considering the application intervals $t_0/2$ and t_2 (yellow area in Fig. 3), leading to

$$\tilde{i}_{pp} = \frac{2}{L}\left\{V_{dc} m \cos\vartheta \frac{t_0}{2} + \left(V_{dc} m \cos\vartheta - \frac{V_{dc}}{3}\right) t_2\right\}. \quad (19)$$

For both cases (18) and (19), introducing the expressions for application intervals $t_0/2$ and t_2, (11) and (12), peak-to-peak current ripple can be written as

$$\tilde{i}_{pp} = \frac{V_{dc} T_s}{2L} r(m, \vartheta)\,, \quad (20)$$

being $r(m,\vartheta)$ the normalized peak-to-peak current ripple amplitude given by

$$r(m,\vartheta) = m\cos\vartheta\left[1 - \sqrt{3} m \sin(\vartheta + 60^\circ)\right], \quad 0 \le m\cos\vartheta \le \frac{1}{3} \quad (21)$$

$$r(m,\vartheta) = m\left\{\cos\vartheta\left[1 - \sqrt{3} m \sin(\vartheta + 60^\circ)\right] + 2\sqrt{3}\sin\vartheta\left(m\cos\vartheta - \frac{1}{3}\right)\right\}, \quad \frac{1}{3} \le m\cos\vartheta \le \frac{1}{\sqrt{3}} \quad (22)$$

2) Evaluation in the range $60° \le \vartheta \le 90°$

Considering the third triangle depicted in Fig. 3, (green area), $60° \le \vartheta \le 90°$, the peak-to-peak current ripple amplitude can be determined considering the application intervals $t_0/2$ and t_2 for all modulation indexes, according to Fig. 6. Introducing (17) in (8) and (9) leads to

$$\tilde{i}_{pp} = \frac{2}{L}\left\{V_{dc} m \cos\vartheta \frac{t_0}{2} + \left[V_{dc} m \cos\vartheta + \frac{1}{3} V_{dc}\right] t_2\right\}. \quad (23)$$

Considering the expressions for application intervals t_0 and t_2, (14) and (15), normalized current ripple amplitude is

$$r(m,\vartheta)=m\left\{\frac{1}{\sqrt{3}}sin\,\vartheta-3m\,cos^2\,\vartheta\right\}. \quad (24)$$

D. Peak-to-peak current ripple diagrams

In order to show the behaviour of the peak-to-peak current ripple amplitude in the fundamental period for all the possible cases, in Figs. 7 and 8 is represented the normalized function $r(m,\vartheta)$ defined by (20). Fig. 7. shows $r(\vartheta)$ for m = 1/6, 1/3, and 1/2, corresponding to the dashed circles in Fig. 3. Since symmetric PWM modulation is considered, ripple is symmetric as well, so the ripple envelope corresponds to the half of $\tilde{i}_{pp}$. The two regions ($0 \le \vartheta \le 60°$ and $60° \le \vartheta \le 90°$) can be distinguished for m = 1/6 and 1/3. All the three regions are visible for m = 1/2, according to Fig. 3.

Fig. 8 shows the colored map of $r(m,\vartheta)$ in 1st quadrant within the modulation limits. The ripple amplitude is almost proportional to m in the neighbourhoods of m = 0. It can be identified a phase angle with minimum ripple, that is $\vartheta \approx 50°\div60°$, and a phase angle with maximum ripple, that is ϑ = 90°. These aspects are developed in the following.

E. Maximum and minimum of the current ripple

In order to estimate current ripple amplitude in the whole fundamental period, the maximum and the minimum of the current ripple can be evaluated. For this purpose, four relevant points can be noticed in Figs. 7 and 8, as mentioned above: two local maxima, for ϑ = 0 and for ϑ = 90°, and two local minima for ϑ = 60° and for $m\,cos\vartheta$ = 1/3, i.e., around ϑ = 50°.

To determine the local maxima, it can be set ϑ = 0 in (21), and ϑ = 90° in (24), leading to the following global maximum

$$r^{max}(m)=max\left\{m\left[1-\frac{3}{2}m\right],\frac{1}{\sqrt{3}}m\right\}. \quad (25)$$

The intersection between the two local maxima gives the border value of modulation index

$$m\left[1-\frac{3}{2}m\right]=\frac{1}{\sqrt{3}}m\,, \quad (26)$$

leading to $m \approx 0.282$. Finally, combining (25) and (26), the maximum of normalized current ripple is

$$r^{max}(m)=\begin{cases} m\left[1-\frac{3}{2}m\right] & \text{for } m<0.282, \\ \frac{1}{\sqrt{3}}m & \text{for } m>0.282. \end{cases} \quad (27)$$

In order to determine the local minima, it is set ϑ = 60° in either (21) or (24), and $m\,cos\vartheta$ = 1/3 in (21). The expression for the global minimum of normalized current ripple is

$$r^{min}(m)=min\left\{m\left[\frac{1}{2}-\frac{3}{4}m\right],\frac{1}{6}\left[1-\sqrt{3m^2-\frac{1}{3}}\right]\right\}. \quad (28)$$

The intersection between the two local minima gives the border value of modulation index

$$m\left[\frac{1}{2}-\frac{3}{4}m\right]=\frac{1}{6}\left[1-\sqrt{3m^2-\frac{1}{3}}\right], \quad (29)$$

leading to $m \approx 0.479$. Finally, combining (28) and (29) the minimum of normalized current ripple is

$$r^{min}(m)=\begin{cases} m\left[\frac{1}{2}-\frac{3}{4}m\right] & \text{for } m<0.479, \\ \frac{1}{6}\left[1-\sqrt{3m^2-\frac{1}{3}}\right] & \text{for } m>0.479. \end{cases} \quad (30)$$

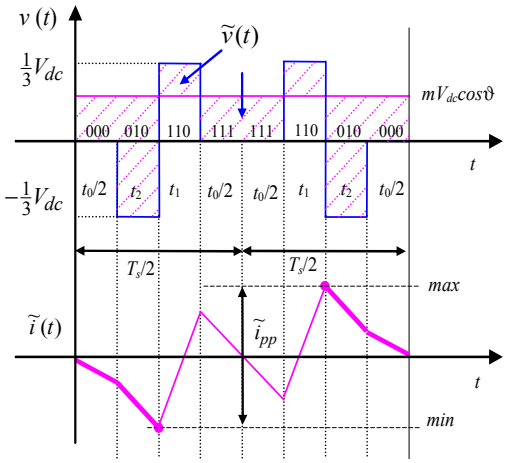

Fig. 6. Output voltage and current ripple in one switching period ($60° \le \vartheta \le 90°$).

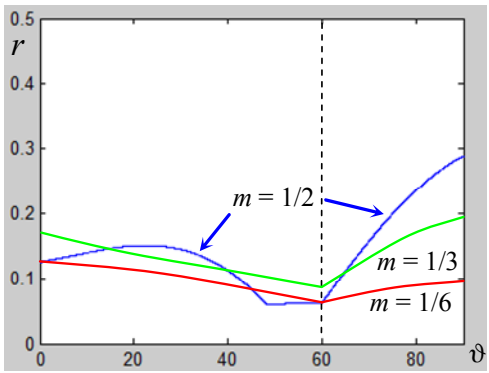

Fig. 7. Normalized peak-to-peak current ripple amplitude $r(m,\vartheta)$ for three modulation indexes, m = 1/6, 1/3, and 1/2, in the phase angle range [0, 90°].

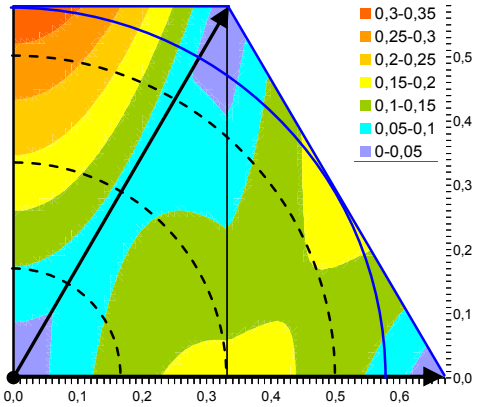

Fig. 8. Map of the normalized peak-to-peak current ripple amplitude $r(m,\vartheta)$.

978-1-4673-4913-0/13/$31.00 ©2013 IEEE

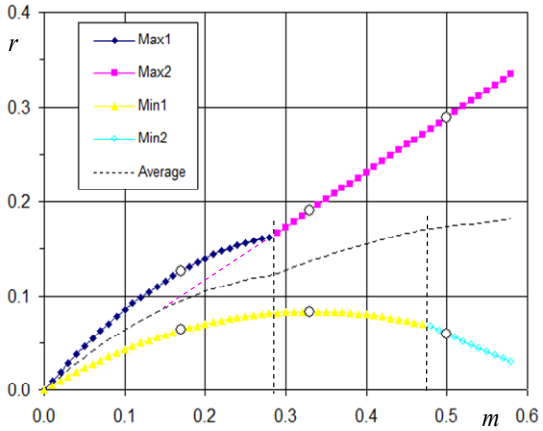

Fig. 9. Maximum and minimum of normalized peak-to-peak current ripple amplitude as function of modulation index.

The composition of the two local minima and maxima are given in Fig. 9, leading to global maximum and minimum. The white dots represent the specific points for m = 1/6, 1/3, and 1/2, displayed in Fig. 7 and further examined in simulations. It can be noted that the maximum function is almost linear for every modulation index, strictly for $m > 0.282$. Then, on the basis of (20) and (27), a simplified expression for maximum of peak-to-peak current ripple amplitude is obtained

$$\tilde{i}_{pp}^{\,max} \cong \frac{V_{dc} T_s}{2\sqrt{3}L} m \ . \tag{31}$$

In [16] this property was recognized and a simplified expression similar to (31) was introduced in the analytical developments to evaluate the current ripple.

III. Numerical Results

In order to verify the theoretical developments shown in previous sections, circuit simulations are carried out by SimPowerSystems of Matlab considering three-phase inverter connected to sinusoidal voltage sources by RL impedance, having R = 0.2 Ω and L = 3 mH. This topology could represent a general three-phase inverter connected to either motor or grid. In all simulations the fundamental frequency is set to 50Hz, the switching frequency $1/T_s$ is 2.1 kHz, and the dc voltage supply V_{dc} is 200V. A continuous symmetrical carrier-based PWM technique is considered, equivalent to the space vector PWM presented in Section II. B.

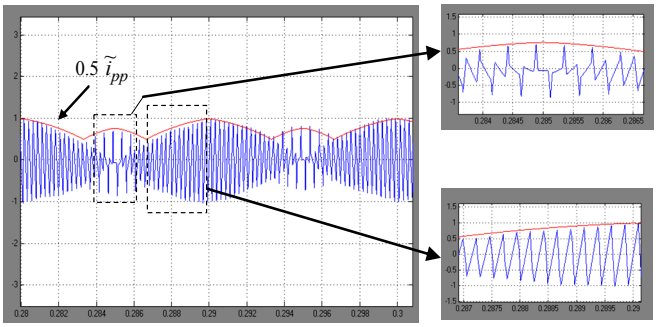

Fig. 10. Current ripple (m = 1/6): simulation results (blue) and evaluated peak-to-peak amplitude (red envelope) for one fundamental period, with details.

The instantaneous current ripple $\tilde{i}$ in simulations is calculated as the difference between the instantaneous current and its fundamental component, i.e.

$$\tilde{i}(t) = i(t) - I_{fund}(t) \ . \tag{32}$$

The three-phase system is well balanced and 1st phase is selected for further analysis, as in analytical approach. Different values of m are investigated (1/6, 1/3, 1/2), as in Section II.

In Figs. 10, 12, and 14 the current ripple $\tilde{i}$ calculated in simulations by (32) (blue trace) is compared with the half of peak-to-peak current ripple, $\tilde{i}_{pp}/2$, evaluated in the different regions by the equations presented in Section II (red trace), for one fundamental period. Each figure is backed with the enlarged detailed view of ripple.

In Figs. 11, 13, and 15 is depicted the instantaneous output current with the calculated upper/lower ripple envelope, depicted in blue/red colors, respectively. To better compare the current waveforms, the fundamental current amplitude is kept constant by adjusting the amplitude of the sinusoidal voltage source (grid).

The agreement is good in the whole fundamental period for all the three considered cases, covering all the colored areas of Fig. 3, providing the effectiveness of the proposed method for calculating the peak-to-peak current ripple amplitude.

IV. Conclusion

In this paper the instantaneous output current ripple in three-phase PWM inverters has been identified and analyzed in details. In particular, the analytical expression of peak-to-peak current ripple amplitude has been derived in the whole fundamental period as function of the modulation index by identifying three different relevant cases.

Furthermore, simplified expressions to evaluate maximum and minimum current ripple amplitude in the fundamental period are given. In particular, it has been pointed out that maximum peak-to-peak current ripple amplitude is almost linear function of modulation index. All analytical developments have been verified with numerical simulations with reference to some relevant cases by a realistic circuit model.

Despite of the proposed analysis is based on continuous symmetric PWM, it can be easily extended to either discontinuous or unsymmetrical modulation, both carrier-based and space vector PWM. Furthermore, the derived

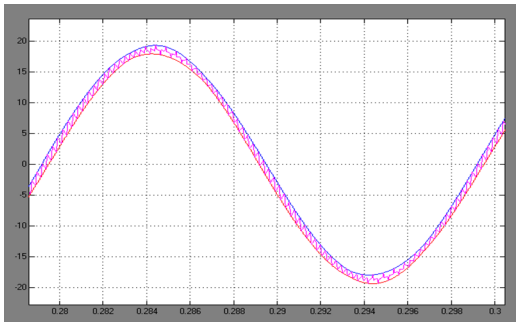

Fig. 11. Instantaneous output current with calculated ripple envelopes (red and blue traces) for m = 1/6.

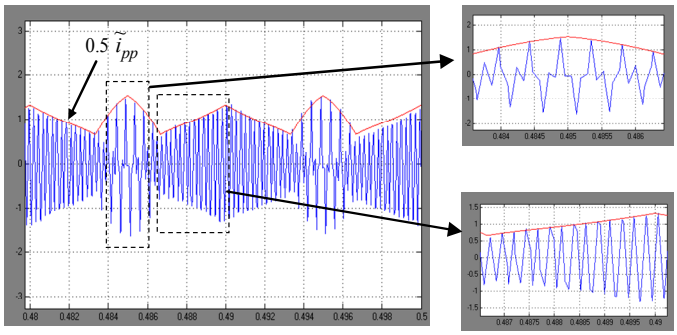

Fig. 12. Current ripple (m = 1/3): simulation results (blue) and evaluated peak-to-peak amplitude (red envelope) for one fundamental period, with details.

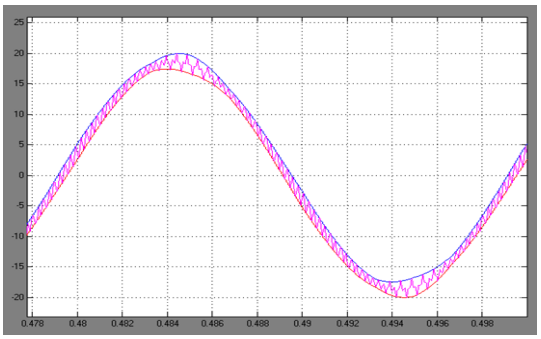

Fig. 13. Instantaneous output current with calculated ripple envelopes (red and blue traces) for m = 1/3.

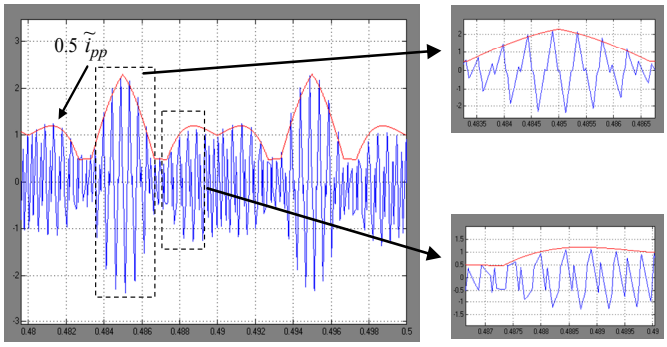

Fig. 14. Current ripple (m = 1/2): simulation results (blue) and evaluated peak-to-peak amplitude (red envelope) for one fundamental period, with details.

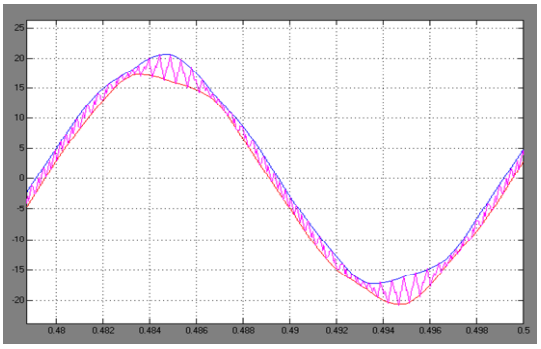

Fig. 15. Instantaneous output current with calculated ripple envelopes (red and blue traces) for m = 1/2.

analytical expressions can be utilized to minimize the peak-to-peak current ripple by properly adjusting the switching frequency and/or the sharing of the null-voltage-vector application time between the two null switch configurations.

REFERENCES

[1] A.M. Hava, R. J. Kerkman, T.A. Lipo, "Carrier-based PWM-VSI overmodulation strategies: analysis, comparison, and design," *IEEE Trans. On Power Electronics*, vol. 13, no. 4, July 1998, pp. 674-689.

[2] D. Zhao, V.S.S. Pavan Kumar Hari, G. Narayanan, R. Ayyanar, "Space-vector hybrid pulsewidth modulation techniques for reduced harmonic distortion and switching loss," *IEEE Trans. On Power Electronics*, vol. 25, no. 3, March 2010, pp. 760-774.

[3] D. Casadei, M. Mengoni, G. Serra, A. Tani, L. Zarri, "A new carrier-based PWM strategy with minimum output current ripple for five-phase inverters," *Power Electronics and Applications (EPE), Proceedings of the 14th European Conference on*, Aug. 30 2011-Sept. 1 2011, pp. 1-10.

[4] X. Mao, R. Ayyanar, H.K. Krishnamurthy, "Optimal variable switching frequency scheme for reducing switching loss in single-phase inverters based on time-domain ripple analysis," *IEEE Trans. On Power Electronics*, vol. 24, no. 4, April 2009, pp. 991-1001.

[5] G.D. Holmes, T.A. Lipo (2003), "Pulse Width Modulation for Power Converters - Principles and Practice," IEEE Press Series on Power Engineering, John Wiley and Sons, Piscataway, NJ, USA.

[6] J. W. Kolar, H. Ertl, F.C. Zach, "Influence of the modulation method on the conduction and switching losses of a PWM converter system," *IEEE Trans. On Industry applications*, vol. 27, no. 6, November/December 1991, pp. 1063-1075.

[7] J.W. Kolar, H. Ertl, F.C. Zach, " Minimizing the current harmonics RMS value of three-phase PWM converter systems by optimal and suboptimal transition between continuous and discontinuous modulation," *Power Electronics Specialists Conference, 1991. PESC '91 Record., 22nd Annual IEEE,* 24-27 Jun 1991, pp. 372 - 381 .

[8] D. Casadei, G. Serra, A. Tani, L. Zarri, "Theoretical and Experimental Analysis for the RMS Current Ripple Minimization in Induction Motor Drives Controlled by SVM Technique," *IEEE Transactions on Industrial Electronics*, vol. 51, no. 5, Oct. 2004.

[9] D. Dujic, M. Jones, E. Levi, "Analysis of output current ripple rms in multiphase drives using space vector approach," *IEEE Trans. On Power Electronics*, vol. 24, no. 8, August 2009, pp. 1926-1938.

[10] M. Jones, D. Dujic, E. Levi, J. Prieto, F. Barrero, "Switching ripple characteristics of space vector PWM schemes for five-phase two-level voltage source inverters-Part2: Current ripple," *IEEE Trans. On Industrial Electronics*, vol. 58, no. 7, July 2011, pp. 2799-2808.

[11] P.A. Dahono, Deni, E.G. Supriatna, "Output current-ripple analysis of five-phase PWM inverters," *IEEE Trans. On Industry Applications*, vol. 45, no. 6, November/December 2009, pp. 2022-2029.

[12] G. Narayanan, D. Zhao, H.K. Krishnamurthy, R. Ayyanar, V.T. Ranganathan, "Space vector based hybrid PWM techniques for reduced current ripple," *IEEE Trans. On Industrial Electronics*, vol. 55, no. 4, April 2008, pp. 1614-1627.

[13] T.B. Reddy, J. Amarnath, D. Subbarayudu, "New hybrid SVPWM methods for direct torque controlled induction motor drive for reduced current ripple," *Power Electronics, Drives and Energy Systems, 2006. PEDES '06. International Conference on*, 12-15 Dec. 2006, pp. 1-6.

[14] A. Murnandityo, P.A. Dahono, "Analysis of output current ripple of three-phase PWM inverter under discontinuous modulation techniques," *Industrial Electronic Seminar*, 2010.

[15] D. Jiang, F. (Fred) Wang, "Study of analytical current ripple of three-phase PWM converter," *Applied Power Electronics Conference and Exposition (APEC), 2012 Twenty-Seventh Annual IEEE*, 5-9 Feb. 2012, pp. 1568 - 1575 .

[16] G. Grandi, J. Loncarski, R. Seebacher, "Effects of current ripple on dead-time distortion in three-phase voltage source inverters," *2nd IEEE ENERGYCON Conference & Exhibition*, 9-12 Sept. 2012.

[17] E. Levi, D. Dujic, M. Jones, G. Grandi, "Analytical Determination of DC-bus Utilization Limits in Multi-Phase VSI Supplied AC Drives," *IEEE Trans. on Energy Convers.*, vol. 23, no. 2, June 2008, pp. 433-443.